Journal of Optics

PAPER

Nonlinear conversion of orbital angular momentum in tungsten disulfide monolayer

IOP Publishing Journal of Optics
J. Opt. 21 (2019) 125404 (8pp) https://doi.org/10.1088/2040-8986/ab5203

Nonlinear conversion of orbital angular momentum in tungsten disulfide monolayer

Arindam Dasgupta, Xiaodong Yang[1] and Jie Gao[1]

Department of Mechanical and Aerospace Engineering, Missouri University of Science and Technology, Rolla, MO 65409, United States of America

E-mail: yangxia@mst.edu and gaojie@mst.edu

Received 30 August 2019, revised 16 October 2019
Accepted for publication 28 October 2019
Published 13 November 2019

Abstract

The unbounded dimension of orbital angular momentum of light has made it one of the most vital parameters to store, control and transport information in optical communication. Along with orbital angular momentum, frequency, polarization and intensity of light are also essential degrees of freedom for encoding and multiplexing data streams in optical and quantum information processing. Therefore, nonlinear generation and conversion of orbital angular momentum have attracted considerable attention in recent years. Here, we theoretically and experimentally demonstrate the nonlinear conversion of orbital angular momentum in atomically thin tungsten disulfide monolayer at both of the second- and third-harmonic frequencies of the fundamental vortex beam. Moreover, we also show that by taking advantage of the symmetry properties of the crystal, the intensity and polarization state of the converted nonlinear vortex beam can be precisely controlled and determined by the polarization state of the fundamental beam. Our results can have a direct implication in building atomically thin optical multiplexers, signal processors, and other prototypes in nonlinear optical conversion for future on-chip photonic circuits, quantum memory and computing devices.

Keywords: 2D materials, tungsten disulfide, elliptical polarization, second-harmonic generation, third-harmonic generation, orbital angular momentum

1. Introduction

The orbital angular momentum (OAM) of light is one of the most important research topics in optical communication and light–matter interaction. In 1992, Allen *et al* first recognized that an optical vortex beam with helical phase dependence of $\exp(il\phi)$ carries the OAM of $l\hbar$ for each photon and possesses the doughnut-shaped spatial profile, with the topological charge (TC) l and the azimuthal angle ϕ [1]. Since then, the unbounded dimension of TC and the unique optical properties of optical vortex beams have been harnessed for various macroscale and on-chip applications such as large-scale optical data transmission [2–4], high-capacity spatial-mode-division multiplexing [5, 6], high-dimensional quantum information processing [7–9], quantum memory [10–12], cryptography [13], and nanoscale optical tweezers [14–18].

Together with orbital angular momentum, frequency, polarization and intensity of light are also considered as some of the important parameters for encoding and multiplexing information in optical communication. The generation and transformation of OAM have been studied through different types of nonlinear optical processes such as second-harmonic generation (SHG) [19–22], third-harmonic generation (THG) [23], sum-frequency generation [24–26], and coherent anti-Stokes Raman scattering [27]. Apart from these, OAM addition and mixing through SHG has also been demonstrated in nonlinear crystals [28–30], plasmonic and dielectric chiral nanostructures [31]. In all the cases, the TC and polarization of the converted beam depend on those of the fundamental laser beam. However, most of these studies only exploited linear and circular polarizations, hence rarely considered elliptically polarized light [32] to explore the possibility of using the parameters of the polarization ellipse as new degrees of freedom for further information encoding and multiplexing. Recently, it has been demonstrated that the propagation characteristics of an elliptically polarized

[1] Authors to whom any correspondence should be addressed.

vortex beam strongly depends on the ellipticity and thus can have many useful implications in long-range and short-range optical communications [33, 34]. Furthermore, most OAM conversion experiments mainly adopted bulky nonlinear crystals as the nonlinear medium [20, 35–37] which hinders the on-chip integration. The use of ultrathin plasmonic metasurfaces has provided a breakthrough in realizing on-chip OAM conversion devices [38–40], but low conversion efficiency and high absorption loss remain a big challenge for their practical implementation.

Recently, nonlinear optics with transition metal dichalcogenide (TMDC) monolayers has drawn broad interest for realizing a wide range of photonic and optoelectronic applications [41–45]. Apart from being a noncentrosymmetric hexagonal lattice (D^1_{3h} space group), the direct bandgap and trigonal wrapping of one metal atom layer between two chalcogen atom layers allow the unique TMDC materials to exhibit strong second-order and third-order susceptibilities at the same time [46–48]. Therefore, TMDC monolayers have not only been demonstrated to be excellent ultrathin nonlinear medium for SHG and THG, but recently spontaneous parametric down-conversion has also been predicted [49, 50]. Moreover, negligible absorption loss and the ability to be easily interfaced at the nanoscale [43, 44] make these atomically thin TMDC monolayer crystals ideal candidates for building on-chip nonlinear photonic devices.

With that hindsight, here we theoretically and experimentally demonstrate the second- and third-harmonic (SH and TH) nonlinear conversion of OAM from only one tungsten disulfide (WS_2) monolayer crystal. In addition to observing the doubling and tripling of OAM during the SH and TH nonlinear conversion, we also investigate how the ellipticity and orientation of the polarization ellipse as well as the intensity variation of the SH and TH vortex beams evolve depending on the polarization state of the fundamental vortex beam. Our results not only provide a better understanding of the light–matter interactions in TMDC monolayers during the nonlinear conversion processes but also can be harnessed to realize efficient frequency-, polarization-, and OAM-based multiplexing, demultiplexing and encoding prototypes for building miniaturized atomic-scale optical communication and computing devices.

2. SHG and THG from WS_2 monolayer

Single-crystal WS_2 monolayer triangles grown by the low-pressure chemical vapor deposition method on a c-cut (0001) sapphire substrate (2D Semiconductors) are used for the experiment. Figure 1(a) is the schematic illustration of the experimental setup. The circularly polarized femtosecond laser beam at the wavelength of 1560 nm (Calmer fiber laser, pulse width 90 fs) is passed through a zero-order vortex half-wave plate (Thorlabs) to generate a Laguerre–Gaussian (LG) beam of TC = 1 which is focused on the WS_2 monolayer sample through a 10× objective lens of numerical aperture (NA) 0.2. The combination of a linear polarizer (LP) and a quarter-wave plate (QWP) is used to obtain the desired polarization state in the fundamental excitation vortex beam. The transmitted beam consisting of fundamental, SHG and THG responses is then

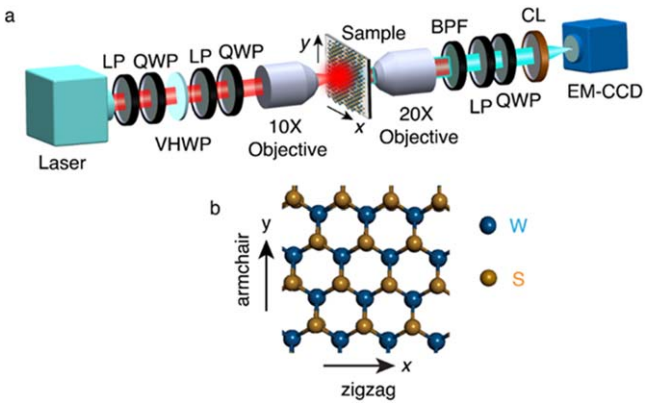

Figure 1. (a) Schematic diagram of the experimental setup. (LP: linear polarizer; QWP: quarter-wave plate; VHWP: vortex half-wave plate; BPF: band-pass filter; CL: cylindrical lens.) (b) Top-view of the WS_2 monolayer crystal lattice. The *y*-direction represents the armchair direction while the *x*-direction corresponds to the zigzag direction along which the mirror symmetry is broken.

collected using another objective lens (20×, 0.42 NA) and focused on an electron multiplying charge-coupled device (EMCCD) camera (Andor iXon) for imaging. The SHG and THG responses are filtered out using 780 nm and 520 nm band-pass filters, respectively. To monitor the spectral profile of the nonlinear signal, an optical spectrometer (iHR 550, Horiba) is used instead of the EMCCD. Figure 1(b) represents the experimental coordinate system in terms of the hexagonal crystal structure of the WS_2 monolayer. While the yellow spheres represent the vertically separated layers of the S atoms, the blue spheres indicate the W atoms. The armchair direction of WS_2 crystal is oriented along the vertical direction (*y*-axis) whereas the zigzag direction with reflection symmetry is along the horizontal direction (*x*-axis).

First, the SHG and THG emission from the WS_2 monolayer is characterized. Figure 2(a) is a transmission-optical microscope image of the WS_2 monolayer used in the experiment. Figure 2(b) shows the dark-field image of the linearly polarized TC = 1 fundamental vortex beam focused on the WS_2 monolayer sample, with the polarization set along the armchair direction of the crystal. Figure 2(c) plots the optical spectrum of the nonlinear signal from the WS_2 monolayer for the pump power of 30 mW where the SHG and THG signals are observed at the wavelengths of 780 nm and 520 nm, respectively. The THG intensity is found to be almost twice of that of the SHG where the THG and SHG conversion efficiency for this particular pump power are estimated to be 1.4×10^{-10} and the 6.3×10^{-11}, respectively. Figure 2(d) shows that the SHG and THG responses follow the expected quadratic and cubic dependences with the pump power, respectively.

3. Theoretical analysis for nonlinear conversion of vortex beam

Next, it is explored how the OAM and polarization properties of the converted nonlinear vortex beam get transformed depending upon the polarization state of fundamental vortex

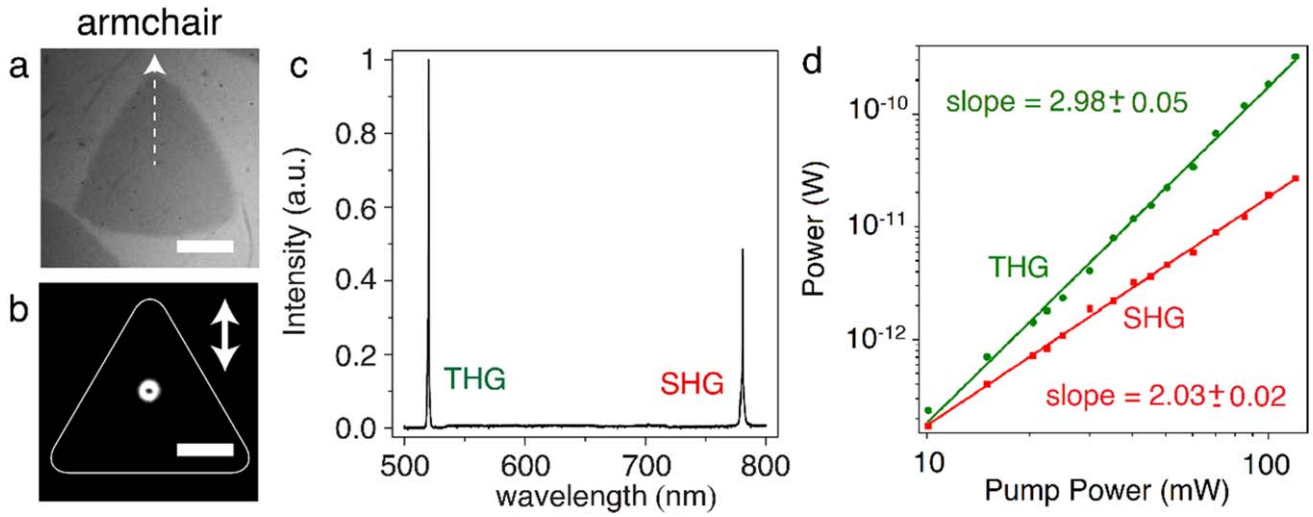

Figure 2. (a) Transmission-optical microscope image of the WS_2 monolayer crystal used in the experiment. The white-dashed arrow represents the armchair direction of the crystal lattice. (b) Dark-field image of the linearly polarized fundamental vortex beam with TC = 1 focused on the WS_2 monolayer sample. The linear polarization is along the armchair direction. Scale bar is 10 μm. (c) The nonlinear response spectrum under fundamental vortex excitation of WS_2 monolayer showing SHG and THG signals at the wavelengths of 780 and 520 nm, respectively. (d) Double log-scale plots of the measured SHG and THG power from WS_2 monolayer as a function of the incident fundamental pump power.

beam. The fundamental pump beam is considered to be an elliptically polarized vortex beam of TC = l_f at the fundamental frequency of ω, where the major axis of the polarization ellipse is oriented along the armchair direction (y-axis) of the crystal, with the electric field expressed as

$$E^{(\omega)} = E_0 \exp\left[-\left(\frac{r^2}{w_f^2} + i l_f \phi\right)\right]\left(\frac{r\sqrt{2}}{w_f}\right)^{l_f} \times \left(\frac{i\epsilon_f}{\sqrt{1+\epsilon_f^2}}\hat{x} \pm \frac{1}{\sqrt{1+\epsilon_f^2}}\hat{y}\right), \quad (1)$$

where r is the radial distance from the beam center, ϕ is the azimuthal angle, w_f is the radius of the Gaussian beam, and ϵ_f defines the ellipticity of the polarization ellipse. $\hat{x}$ and $\hat{y}$ are the unit vectors in the experimental coordinate system as defined in figure 1.

Now, SHG from the WS_2 monolayer is related to both the incident electric field and the second-order nonlinear susceptibility ($\chi^{(2)}$) tensor of the crystal. Assuming that the crystallographic coordinate system is defined by (x, y, z) as shown in figure 1, $\chi^{(2)}$ can be defined as

$$\chi^{(2)} = \begin{pmatrix} \chi_{11}^{(2)} & \chi_{12}^{(2)} & \chi_{13}^{(2)} & \chi_{14}^{(2)} & \chi_{15}^{(2)} & \chi_{16}^{(2)} \\ \chi_{21}^{(2)} & \chi_{22}^{(2)} & \chi_{23}^{(2)} & \chi_{24}^{(2)} & \chi_{25}^{(2)} & \chi_{26}^{(2)} \\ \chi_{31}^{(2)} & \chi_{32}^{(2)} & \chi_{33}^{(2)} & \chi_{34}^{(2)} & \chi_{35}^{(2)} & \chi_{36}^{(2)} \end{pmatrix}, \quad (2)$$

where the first subscripts 1, 2, 3 refer to x, y, z respectively and the second subscript signifies the following:

$$\begin{matrix} 1 & 2 & 3 & 4 & 5 & 6 \\ xx & yy & zz & yz & zx & xy. \end{matrix}$$

Since the WS_2 monolayer belongs to the D_{3h}^1 space group, there is only one independent nonvanishing $\chi^{(2)}$ tensor element [51]:

$$\chi_{yyy}^{(2)} = -\chi_{yxx}^{(2)} = -\chi_{xxy}^{(2)} = -\chi_{xyx}^{(2)} = \chi_{22}^{(2)}. \quad (3)$$

Therefore, the second-order nonlinear polarization components in WS_2 monolayer is expressed as

$$\begin{bmatrix} P_x^{(2\omega)} \\ P_y^{(2\omega)} \\ P_z^{(2\omega)} \end{bmatrix} = \varepsilon_0 \begin{pmatrix} 0 & 0 & 0 & 0 & 0 & -\chi_{22}^{(2)} \\ -\chi_{22}^{(2)} & \chi_{22}^{(2)} & 0 & 0 & 0 & 0 \\ 0 & 0 & 0 & 0 & 0 & 0 \end{pmatrix} \times \begin{bmatrix} E_x^{(\omega)2} \\ E_y^{(\omega)2} \\ E_z^{(\omega)2} \\ 2E_y^{(\omega)}E_z^{(\omega)} \\ 2E_z^{(\omega)}E_x^{(\omega)} \\ 2E_x^{(\omega)}E_y^{(\omega)} \end{bmatrix} \quad (4)$$

which yields the expression of the second-order nonlinear polarization as

$$P^{(2\omega)} = \begin{bmatrix} P_x^{(2\omega)} \\ P_y^{(2\omega)} \\ P_z^{(2\omega)} \end{bmatrix} = \varepsilon_0 \chi_{22}^{(2)} \begin{pmatrix} -2E_x E_y \\ -E_x^2 + E_y^2 \\ 0 \end{pmatrix}. \quad (5)$$

Correspondingly, SH electric field can be expressed as $E^{(2\omega)} \propto P_x^{(2\omega)}\hat{x} + P_y^{(2\omega)}\hat{y}$ and thus by using equations (1) and (5), the expression of the SH vortex beam is obtained as

$$E^{(2\omega)} \propto \varepsilon_0 \chi_{22}^{(2)} E_0^2 \exp\left[-\left(\frac{r^2}{w_2^2} + il_2\phi\right)\right] \times \left(\frac{r\sqrt{2}}{w_f}\right)^{l_2}\left(\mp\frac{i2\epsilon_f}{1+\epsilon_f^2}\hat{x} + \hat{y}\right). \quad (6)$$

Therefore, the SHG of a fundamental vortex beam with arbitrary elliptical polarization will generate a vortex beam with the doubled TC $l_2 = 2l_f$ and a reduced $w_2 = w_f/\sqrt{2}$. Equation (6) also indicates that the ellipticity of the SH vortex beam ϵ_{SHG} is transformed from that of the fundamental vortex beam into the following

$$\epsilon_{SHG} = -\frac{2\epsilon_f}{1+\epsilon_f^2} \quad (7)$$

while the orientation of the polarization ellipse remains unchanged along the armchair direction. Note that a different scenario can occur if the fundamental vortex beam has an elliptical polarization oriented along the zigzag direction. In that case, a 90° rotation of the SHG polarization ellipse from the polarization orientation of the fundamental beam is expected, which can be attributed to the reflection symmetry in the crystal along the zigzag direction. In equation (7), the change in the sign of the ellipticity means that the handedness of the SH polarization ellipse is flipped, which is generally expected for any noncentrosymmetric crystal with three-fold rotational symmetry. Moreover, equation (6) suggests that the intensity of the SH signal depends on the ellipticity of the fundamental pump beam by the relation of $I_{SHG} \propto (1 + \sin^2 2\beta_f)$ where $\beta_f = \tan^{-1}\epsilon_f$ is the ellipticity angle. Thereby, the intensity of the SH vortex beam under the circularly polarized fundamental excitation with $\beta_f = 45° + m \cdot 90°$ is expected to be twice of that under the linearly polarized excitation with $\beta_f = 0° + m \cdot 90°$.

Similarly, the THG from the WS_2 monolayer in case of the fundamental vortex excitation will depend on the third-order nonlinear susceptibility of the material which is represented by

$$\chi^{(3)} = \begin{pmatrix} \chi_{11}^{(3)} & \chi_{12}^{(3)} & \chi_{13}^{(3)} & \chi_{14}^{(3)} & \chi_{15}^{(3)} & \chi_{16}^{(3)} & \chi_{17}^{(3)} & \chi_{18}^{(3)} & \chi_{19}^{(3)} & \chi_{10}^{(3)} \\ \chi_{21}^{(3)} & \chi_{22}^{(3)} & \chi_{23}^{(3)} & \chi_{24}^{(3)} & \chi_{25}^{(3)} & \chi_{26}^{(3)} & \chi_{27}^{(3)} & \chi_{28}^{(3)} & \chi_{29}^{(3)} & \chi_{20}^{(3)} \\ \chi_{31}^{(3)} & \chi_{32}^{(3)} & \chi_{33}^{(3)} & \chi_{34}^{(3)} & \chi_{35}^{(3)} & \chi_{36}^{(3)} & \chi_{37}^{(3)} & \chi_{38}^{(3)} & \chi_{39}^{(3)} & \chi_{30}^{(3)} \end{pmatrix} \quad (8)$$

with the first subscripts 1, 2, 3 representing the crystallographic axes x, y, z and the second subscript signifying:

1	2	3	4	5	6	7	8	9	0
xxx	*yyy*	*zzz*	*yzz*	*yyz*	*xzz*	*xxz*	*xyy*	*xxy*	*xyz*.

Due to the D_{3h}^1 symmetry of the WS_2 monolayer crystal, there is only one independent nonvanishing $\chi^{(3)}$ tensor element represented as [51, 52]

$$\chi_{11}^{(3)} = \chi_{22}^{(3)} = 3\chi_{18}^{(3)} = 3\chi_{29}^{(3)}. \quad (9)$$

Thus, the third-order nonlinear polarization of the WS_2 monolayer is given by

$$\begin{bmatrix} P_X^{(3\omega)} \\ P_Y^{(3\omega)} \\ P_Z^{(3\omega)} \end{bmatrix} = \begin{pmatrix} \chi_{11}^{(3)} & 0 & 0 & 0 & 0 & \frac{\chi_{11}^{(3)}}{3} & 0 & \frac{\chi_{11}^{(3)}}{3} & 0 & 0 \\ 0 & \chi_{11}^{(3)} & 0 & \frac{\chi_{11}^{(3)}}{3} & 0 & 0 & \frac{\chi_{11}^{(3)}}{3} & 0 & \frac{\chi_{11}^{(3)}}{3} & 0 \\ 0 & 0 & \chi_{11}^{(3)} & 0 & \frac{\chi_{11}^{(3)}}{3} & 0 & \frac{\chi_{11}^{(3)}}{3} & 0 & 0 & 0 \end{pmatrix} \times \begin{pmatrix} E_x^{(\omega)3} \\ E_y^{(\omega)3} \\ E_z^{(\omega)3} \\ 3E_y^{(\omega)}E_z^{(\omega)}E_z^{(\omega)} \\ 3E_z^{(\omega)}E_y^{(\omega)}E_y^{(\omega)} \\ 3E_x^{(\omega)}E_z^{(\omega)}E_z^{(\omega)} \\ 3E_x^{(\omega)}E_x^{(\omega)}E_z^{(\omega)} \\ 3E_x^{(\omega)}E_y^{(\omega)}E_y^{(\omega)} \\ 3E_x^{(\omega)}E_x^{(\omega)}E_y^{(\omega)} \\ 6E_x^{(\omega)}E_y^{(\omega)}E_z^{(\omega)} \end{pmatrix} \quad (10)$$

and the electric field of the TH vortex beam has the form

$$E^{(3\omega)} \propto \varepsilon_0 \chi_{11}^{(3)} E_0^3 \exp\left[-\left(\frac{r^2}{w_3^2} + il_3\phi\right)\right]\left(\frac{r\sqrt{2}}{w_f}\right)^{l_3}\frac{1-\epsilon_f^2}{1+\epsilon_f^2} \times \left(\frac{i\epsilon_f}{\sqrt{1+\epsilon_f^2}}\hat{x} \pm \frac{1}{\sqrt{1+\epsilon_f^2}}\hat{y}\right). \quad (11)$$

This indicates that the TH vortex beam will have the TC $l_3 = 3l_f$ with a reduced w_3 by a factor of $\sqrt{3}$ from w_f. Unlike the SH vortex beam, the TH vortex beam has the same polarization state as the fundamental vortex beam and the intensity is given by $I_{THG} \propto \cos^2 2\beta_f$. Hence, it implies a maximum TH intensity in case of the linearly polarized fundamental excitation as well as a vanishing THG intensity in response to the circularly polarized excitation.

4. Measurements for nonlinear conversion of vortex beam

The intensity profiles of the converted SH and TH vortex beams from the WS_2 monolayer are measured with linearly polarized fundamental vortex beam with TC = 1 where the incident polarization is set along the armchair direction of the crystal. Figure 3(a) is the recorded transmission image of the doughnut-shaped intensity pattern for the fundamental vortex beam. The associated TC of the fundamental vortex beam is confirmed by performing an astigmatic transformation of the recorded image using a cylindrical lens placed

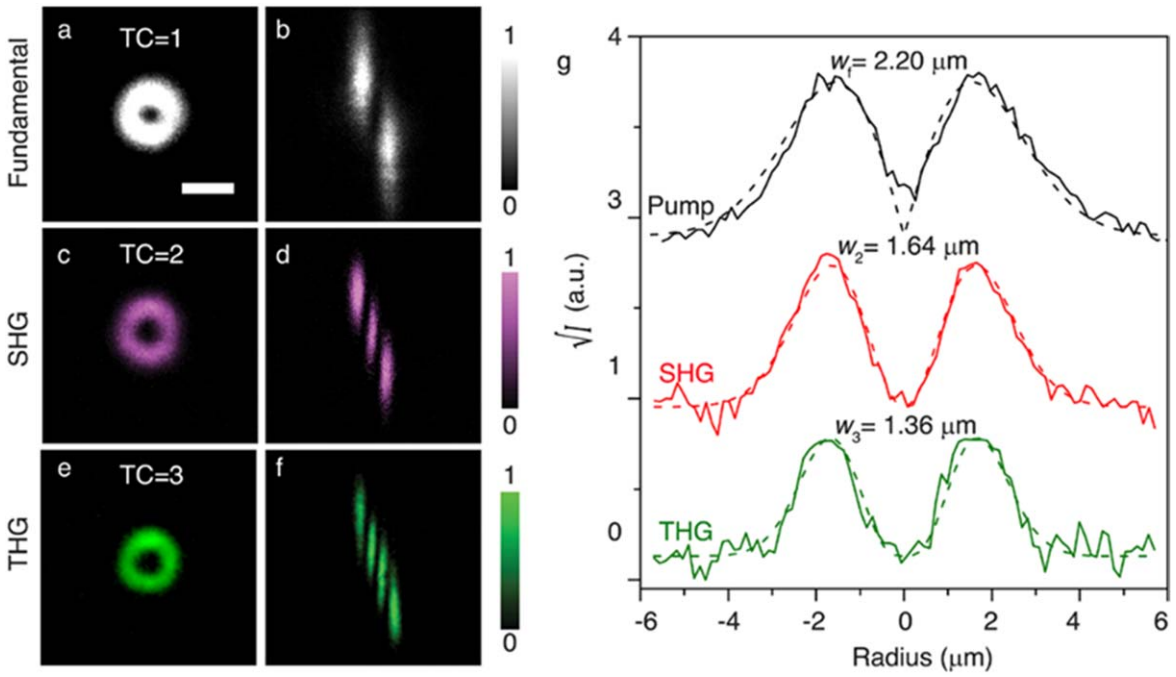

Figure 3. (a) EMCCD image of the fundamental vortex beam with TC = 1 focused on the WS_2 monolayer sample. Scale bar is 5 μm. (b) Cylindrical lens image of the fundamental vortex beam confirming the TC to be 1. (c) False-color EMCCD image of the converted SH vortex beam. (d) Cylindrical lens image of the SH vortex beam indicating the TC to be 2. (e), (f) False-color EMCCD images of the converted TH vortex beam showing the TC to be 3. (g) Measured line profiles of the square root of intensity for the fundamental, SH and TH vortex beams with TC = 1, 2 and 3 (solid curves), fitted by the calculated electric field profiles of $E^{(\omega)}$, $E^{(2\omega)}$ and $E^{(3\omega)}$ (dashed curves).

before the EMCCD. During the astigmatic transformation, the high-TC optical vortex splits into its constituent elementary vortices with TC = 1 to form an extended pattern of tilted dark stripes near the focal plane of the cylindrical lens. The number of dark stripes in the cylindrical lens converted image indicates the TC of the vortex beam [53]. Figure 3(b) shows that the fundamental pump beam has TC = 1. Figure 3(c) gives the recorded image of the SH vortex beam from the WS_2 monolayer and the corresponding cylindrical lens image in figure 3(d) confirms that the SH vortex beam has TC = 2. Similarly, figures 3(e) and (f) show that the converted TH vortex beam has TC = 3. Figure 3(g) further plots the measured line profiles of the square root of intensity for the fundamental, SH and TH vortex beams, which are fitted by the calculated electric field profiles of $E^{(\omega)}$, $E^{(2\omega)}$ and $E^{(3\omega)}$, respectively. It indicates that the measured $\frac{w_2}{w_1}$= 0.75 and $\frac{w_3}{w_1} = 0.62$ which are close to the expected values of $\frac{1}{\sqrt{2}}$ and $\frac{1}{\sqrt{3}}$.

Next, the dependence of the SH and TH vortex intensity on the ellipticity of the fundamental vortex beam is characterized. The desired incident elliptical polarization of the fundamental vortex beam is obtained by placing a linear polarizer along the armchair direction (y-axis) of the WS_2 crystal and a rotating QWP. Depending on the rotation angle β_f between the linear polarizer and the QWP fast axis, the fundamental vortex beam varies from linearly polarized ($\beta_f = 0° + m \cdot 90°$) to circularly polarized ($\beta_f = 45° + m \cdot 90°$). The polar plot in figure 4(a) shows the evolution of the SH vortex intensity as a function of the ellipticity angle β_f. The observed nearly doubled intensity under the circularly polarized excitation compared to that of the linearly polarized excitation is in good agreement with the theoretical prediction of $I_{SHG} \propto (1 + \sin^2 2\beta_f)$. The ellipticity ϵ_{SHG} of the SH vortex beam as a function of the ellipticity ϵ_f of the fundamental vortex beam is also measured by using the Stokes parameters of the SH signals as $S_0 = |E_x^{(2\omega)}|^2 + |E_y^{(2\omega)}|^2$, $S_1 = |E_x^{(2\omega)}|^2 - |E_y^{(2\omega)}|^2$, $S_2 = 2\mathrm{Re}\{E_x^{(2\omega)}E_y^{(2\omega)}\}$ and $S_3 = -2\mathrm{Im}\{E_x^{(2\omega)}E_y^{(2\omega)}\}$, from where the ellipticity angle and the orientation can be obtained as $\beta_{SHG} = \frac{1}{2}\sin^{-1}\left(\frac{S_3}{S_0}\right)$ and $\theta_{SHG} = \frac{1}{2}\tan^{-1}\left(\frac{S_2}{S_1}\right)$, respectively. The ellipticity of the SH vortex beam is then calculated as $\epsilon_{SHG} = \tan\beta_{SHG}$. As shown in figure 4(b), when ϵ_f is gradually changed from −1 to +1 with $\beta_f = -45°$ to 45° signifying from right-handed circular polarization to left-handed circular polarization, the measured ϵ_{SHG} is always opposite to ϵ_f and is consistent with the theoretical calculation shown in equation (7). The slight deviation of the experimental values from the theoretical calculations may be attributed to the defects and deformation in the WS_2 monolayer crystal. Figure 4(c) plots the variation of the TH vortex intensity as a function of the ellipticity angle β_f, showing that the THG signal follows the theoretical prediction of $I_{THG} \propto \cos^2 2\beta_f$, which has a maximum under the linearly polarized fundamental excitation and nearly vanishes under the circularly polarized excitation. As plotted in figure 4(d), the measured ϵ_{THG} of the TH vortex beam is found to be almost the same as ϵ_f of the fundamental vortex beam, which matches with the theoretical calculation of $\epsilon_{THG} = \epsilon_f$.

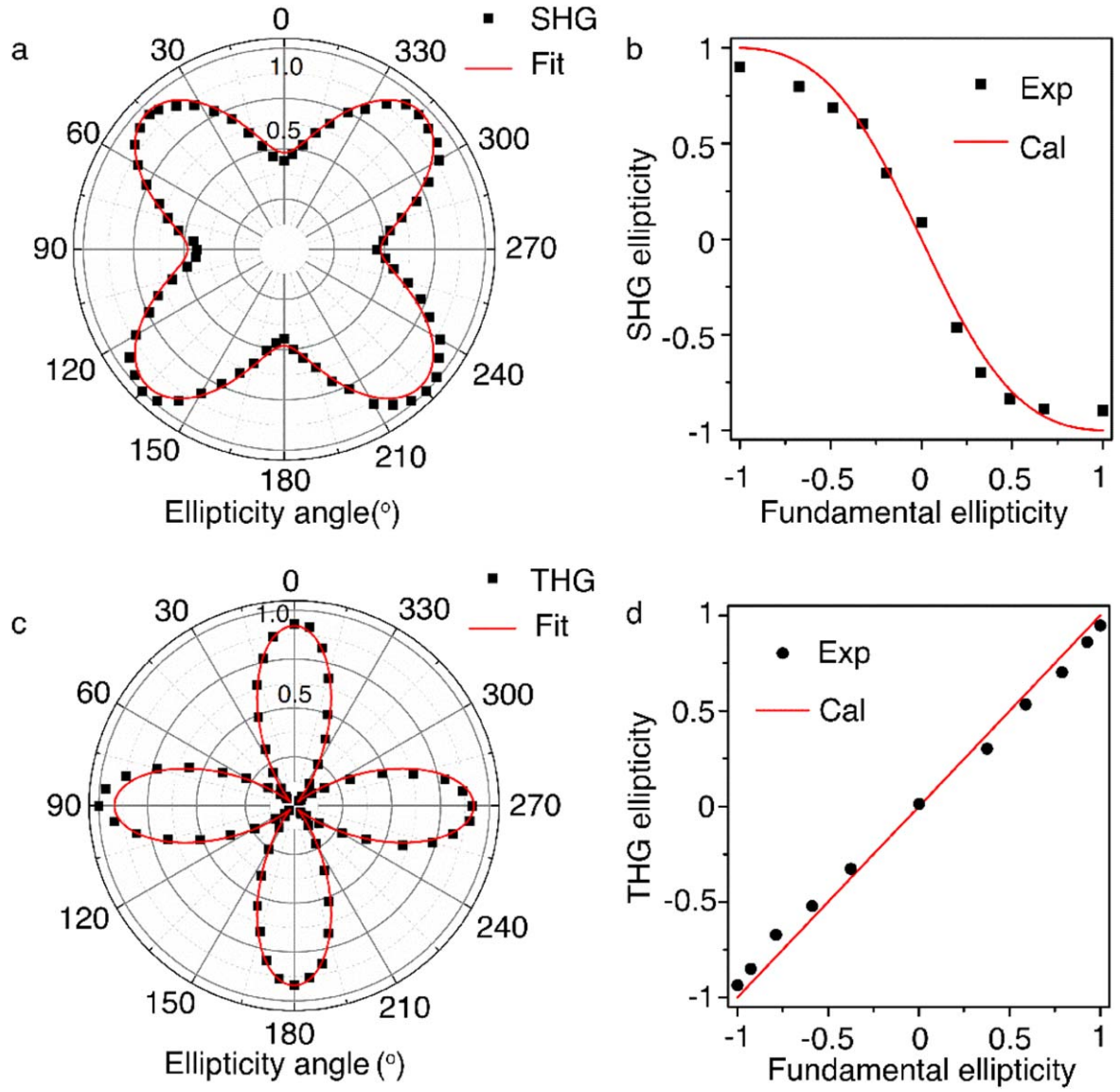

Figure 4. Dependence of the SH vortex intensity on the ellipticity angle β_f of the fundamental vortex beam. 0°, 90°, 180° and 270° correspond to the linear polarization whereas 45°, 135°, 225° and 315° correspond to the circular polarization. The measured data are fitted with $(1 + \sin^2 2\beta_f)$. (b) Evolution of the SH vortex ellipticity ϵ_{SHG} as a function of the ellipticity ϵ_f of the fundamental vortex beam. (c) Dependence of the TH vortex intensity on β_f. The measured data are fitted with $\cos^2 2\beta_f$. (d) Evolution of the TH vortex ellipticity ϵ_{THG} as a function of ϵ_f.

5. Conclusion

In summary, we have theoretically and experimentally demonstrated the nonlinear conversion of the elliptically polarized fundamental vortex beam from atomically thin WS_2 monolayer through both SHG and THG processes. It is shown that the TCs of the converted SH and TH vortex beams get doubled and tripled, respectively. Moreover, it is demonstrated that the intensity and polarization properties of the nonlinear vortex beams can be precisely controlled by the polarization state of the fundamental vortex beam due to the symmetry properties of the WS_2 monolayer crystal. The fact that the same TMDC monolayer crystal can be used for both SH and TH vortex beam conversion with the determined OAMs and the well-specified polarization and intensity makes the TMDC monolayers an effective platform for making nonlinear optical devices used for efficient frequency-, polarization-, and OAM-based multiplexing, demultiplexing and encoding information in optical communication and quantum information processing. In addition to that, the TMDC monolayers with atomic-scale thickness can be harnessed for future on-chip nonlinear applications in integrated photonic circuits and quantum memory devices.

Acknowledgments

The authors acknowledge support from the National Science Foundation under Grant Nos. ECCS-1653032 and DMR-

1552871, and the Office of Naval Research under Grant No. N00014-16-1-2408.

ORCID iDs

Xiaodong Yang https://orcid.org/0000-0001-9031-3155

References

[1] Allen L, Beijersbergen M W, Spreeuw R J C and Woerdman J P 1992 Orbital angular momentum of light and the transformation of Laguerre–Gaussian laser modes *Phys. Rev.* A **45** 8185–9

[2] Yu S 2015 Potentials and challenges of using orbital angular momentum communications in optical interconnects *Opt. Express* **23** 3075–87

[3] Wang J *et al* 2012 Terabit free-space data transmission employing orbital angular momentum multiplexing *Nat. Photon.* **6** 488

[4] Bozinovic N, Yue Y, Ren Y, Tur M, Kristensen P, Huang H, Willner A E and Ramachandran S 2013 Terabit-scale orbital angular momentum mode division multiplexing in fibers *Science* **340** 1545–8

[5] Deng D, Li Y, Zhao H, Han Y, Ye J and Qu S 2019 High-capacity spatial-division multiplexing with orbital angular momentum based on multi-ring fiber *J. Opt.* **21** 055601

[6] Trichili A, Park K, Zghal M, Ooi B S and Alouini M 2019 Communicating using spatial mode multiplexing: potentials, challenges and perspectives *IEEE Commun. Surv. Tutorials* 1–1

[7] Nagali E, Sansoni L, Sciarrino F, De Martini F, Marrucci L, Piccirillo B, Karimi E and Santamato E 2009 Optimal quantum cloning of orbital angular momentum photon qubits through Hong–Ou–Mandel coalescence *Nat. Photon.* **3** 720

[8] Vaziri A, Weihs G and Zeilinger A 2002 Experimental two-photon, three-dimensional entanglement for quantum communication *Phys. Rev. Lett.* **89** 240401

[9] Mair A, Vaziri A, Weihs G and Zeilinger A 2001 Entanglement of the orbital angular momentum states of photons *Nature* **412** 313–6

[10] Ding D-S, Zhang W, Shi S, Zhou Z-Y, Li Y, Shi B-S and Guo G-C 2016 High-dimensional entanglement between distant atomic-ensemble memories *Light: Sci. Appl.* **5** e16157

[11] Nicolas A, Veissier L, Giner L, Giacobino E, Maxein D and Laurat J 2014 A quantum memory for orbital angular momentum photonic qubits *Nat. Photon.* **8** 234

[12] Ding D-S, Zhang W, Zhou Z-Y, Shi S, Pan J-S, Xiang G-Y, Wang X-S, Jiang Y-K, Shi B-S and Guo G-C 2014 Toward high-dimensional-state quantum memory in a cold atomic ensemble *Phys. Rev.* A **90** 042301

[13] Vaziri A, Weihs G and Zeilinger A 2002 Superpositions of the orbital angular momentum for applications in quantum experiments *J. Opt. B: Quantum Semiclass. Opt.* **4** S47–51

[14] Paterson L, MacDonald M P, Arlt J, Sibbett W, Bryant P and Dholakia K 2001 Controlled rotation of optically trapped microscopic particles *Science* **292** 912–4

[15] Curtis J E and Grier D G 2003 Structure of optical vortices *Phys. Rev. Lett.* **90** 133901

[16] Yan Z and Scherer N F 2013 Optical vortex induced rotation of silver nanowires *J. Phys. Chem. Lett.* **4** 2937–42

[17] Padgett M and Bowman R 2011 Tweezers with a twist *Nat. Photon.* **5** 343

[18] He H, Friese M E J, Heckenberg N R and Rubinsztein-Dunlop H 1995 Direct observation of transfer of angular momentum to absorptive particles from a laser beam with a phase singularity *Phys. Rev. Lett.* **75** 826–9

[19] Courtial J, Dholakia K, Allen L and Padgett M J 2002 Second-harmonic generation and the conservation of orbital angular momentum with high-order Laguerre–Gaussian modes *Phys. Rev.* A **56** 4193–6

[20] Bloch N V, Shemer K, Shapira A, Shiloh R, Juwiler I and Arie A 2012 Twisting light by nonlinear photonic crystals *Phys. Rev. Lett.* **108** 233902

[21] Yao A M and Padgett M J 2011 Orbital angular momentum: origins, behavior and applications *Adv. Opt. Photon.* **3** 161–204

[22] Yusufu T, Sasaki Y, Araki S, Miyamoto K and Omatsu T 2016 Beam propagation of efficient frequency-doubled optical vortices *Appl. Opt.* **55** 5263–6

[23] Olivier N and Beaurepaire E 2008 Third-harmonic generation microscopy with focus-engineered beams: a numerical study *Opt. Express* **16** 14703–15

[24] Alexander T J, Kivshar Y S, Buryak A V and Sammut R A 2000 Optical vortex solitons in parametric wave mixing *Phys. Rev.* E **61** 2042–9

[25] Li Y, Zhou Z-Y, Ding D-S and Shi B-S 2015 Sum frequency generation with two orbital angular momentum carrying laser beams *J. Opt. Soc. Am.* B **32** 407–11

[26] Li Y, Zhou Z-Y, Ding D-S and Shi B-S 2016 Dynamic mode evolution and phase transition of twisted light in nonlinear process *J. Mod. Opt.* **63** 2271–8

[27] Zhdanova A A, Shutova M, Bahari A, Zhi M and Sokolov A V 2015 Topological charge algebra of optical vortices in nonlinear interactions *Opt. Express* **23** 34109–17

[28] Buono W T, Moraes L F C, Huguenin J A O, Souza C E R and Khoury A Z 2014 Arbitrary orbital angular momentum addition in second harmonic generation *New J. Phys.* **16** 093041

[29] Pereira L J, Buono W T, Tasca D S, Dechoum K and Khoury A Z 2017 Orbital-angular-momentum mixing in type-II second-harmonic generation *Phys. Rev.* A **96** 053856

[30] Buono W T, Santiago J, Pereira L J, Tasca D S, Dechoum K and Khoury A Z 2018 Polarization-controlled orbital angular momentum switching in nonlinear wave mixing *Opt. Lett.* **43** 1439–42

[31] Xiong X Y Z, Al-Jarro A, Jiang L J, Panoiu N C and Sha W E I 2017 Mixing of spin and orbital angular momenta via second-harmonic generation in plasmonic and dielectric chiral nanostructures *Phys. Rev.* B **95** 165432

[32] Liu T, Gu B, Rui G, Lv C, He J and Cui Y 2019 Conservation of the spin angular momentum in second-harmonic generation with elliptically polarized vortex beams *Appl. Phys. Lett.* **114** 101101

[33] Ou J, Jiang Y and He Y 2015 Intensity and polarization properties of elliptically polarized vortex beams in turbulent atmosphere *Opt. Laser Technol.* **67** 1–7

[34] Chen B and Pu J 2009 Tight focusing of elliptically polarized vortex beams *Appl. Opt.* **48** 1288–94

[35] Fang X, Wei D, Liu D, Zhong W, Ni R, Chen Z, Hu X, Zhang Y, Zhu S and Xiao M 2015 Multiple copies of orbital angular momentum states through second-harmonic generation in a two-dimensional periodically poled $LiTaO_3$ crystal *Appl. Phys. Lett.* **107** 161102

[36] Zhou Z-Y, Ding D-S, Jiang Y-K, Li Y, Shi S, Wang X-S and Shi B-S 2014 Orbital angular momentum light frequency conversion and interference with quasi-phase matching crystals *Opt. Express* **22** 20298–310

[37] Dholakia K, Simpson N B, Padgett M J and Allen L 1996 Second-harmonic generation and the orbital angular momentum of light *Phys. Rev.* A **54** R3742–5

[38] Keren-Zur S, Avayu O, Michaeli L and Ellenbogen T 2016 Nonlinear beam shaping with plasmonic metasurfaces *ACS Photonics* **3** 117–23

[39] Karimi E, Schulz S A, De Leon I, Qassim H, Upham J and Boyd R W 2014 Generating optical orbital angular momentum at visible wavelengths using a plasmonic metasurface *Light-Sci Appl.* **3** e167
[40] Wang Y, Wei D, Zhu Y, Huang X, Fang X, Zhong W, Wang Q, Zhang Y and Xiao M 2016 Conversion of the optical orbital angular momentum in a plasmon-assisted second-harmonic generation *Appl. Phys. Lett.* **109** 081105
[41] Choi W, Choudhary N, Han G H, Park J, Akinwande D and Lee Y H 2002 Recent development of two-dimensional transition metal dichalcogenides and their applications *Mater. Today* **20** 116–30
[42] Gong C, Zhang Y, Chen W, Chu J, Lei T, Pu J, Dai L, Wu C, Cheng Y and Zhai T 2017 Electronic and optoelectronic applications based on 2D novel anisotropic transition metal dichalcogenides *Adv. Sci.* **4** 1700231
[43] Seyler K L, Schaibley J R, Gong P, Rivera P, Jones A M, Wu S, Yan J, Mandrus D G, Yao W and Xu X 2015 Electrical control of second-harmonic generation in a WSe2 monolayer transistor *Nat. Nanotechnol.* **10** 407
[44] Mak K F and Shan J 2016 Photonics and optoelectronics of 2D semiconductor transition metal dichalcogenides *Nat. Photon.* **10** 216
[45] Krasnok A, Lepeshov S and Alú A 2018 Nanophotonics with 2D transition metal dichalcogenides [Invited] *Opt. Express* **26** 15972–94
[46] Säynätjoki A *et al* 2017 Ultra-strong nonlinear optical processes and trigonal warping in MoS_2 layers *Nat. Commun.* **8** 893
[47] Autere A *et al* 2002 Optical harmonic generation in monolayer group-VI transition metal dichalcogenides *Phys. Rev.* B **98** 115426
[48] Rosa H G, Ho Y W, Verzhbitskiy I, Rodrigues M J F L, Taniguchi T, Watanabe K, Eda G, Pereira V M and Gomes J C V 2018 Characterization of the second- and third-harmonic optical susceptibilities of atomically thin tungsten diselenide *Sci. Rep.* **8** 10035
[49] Dinparasti Saleh H, Vezzoli S, Caspani L, Branny A, Kumar S, Gerardot B D and Faccio D 2018 Towards spontaneous parametric down conversion from monolayer MoS_2 *Sci. Rep.* **8** 3862
[50] Marini L G, Helt Y, Lu B J, Eggleton and Palomba S 2002 Constraints on downconversion in atomically thick films *J. Opt. Soc. Am.* B **35** 672–9
[51] Boyd R W 2003 *Nonlinear Optics* (Amsterdam: Elsevier)
[52] Yang X-L and Xie S-W 1995 Expression of third-order effective nonlinear susceptibility for third-harmonic generation in crystals *Appl. Opt.* **34** 6130–5
[53] Denisenko V, Shvedov V, Desyatnikov A S, Neshev D N, Krolikowski W, Volyar A, Soskin M and Kivshar Y S 2009 Determination of topological charges of polychromatic optical vortices *Opt. Express* **17** 23374–9